Transport properties of WSe_2 nanotube heterojunctions: A first-principles study

Zhizhou Yu and Jian Wang*

Department of Physics and the Center of Theoretical and Computational Physics, The University of Hong Kong, Pokfulam Road, Hong Kong, China and The University of Hong Kong Shenzhen Institute of Research and Innovation, Shenzhen, China

(Received 5 October 2014; revised manuscript received 7 May 2015; published 21 May 2015)

Using the nonequilibrium Green's function method within the framework of density functional theory, we investigate various transport properties, such as I-V characteristics, shot noise, thermopower, dynamical conductance, of Au- and Na-encapsulated WSe_2 nanotube heterojunctions. First-principles transport calculations show that from I-V curves large rectification ratio is found in the (8,0) heterojunction and for shot noise it exhibits sub-Poissonian behaviors under positive biases (on Au-encapsulated tubes) while Poissonian behaviors are found under negative biases. For thermopower, it is found that as one sweeps the Fermi energy, the thermopower can change its sign. For dynamic conductance, the (5,5) heterojunction exhibits capacitivelike behavior. We find that the spin-orbit interaction (SOI) is very important for WSe_2 nanotubes. Due to the band splitting originated from SOI, the intrinsic band gap of Au-doped (5,5) nanotube is reduced by about 58% and that of the Na-doped system vanishes, while that of the doped (8,0) nanotubes decreases by about 40%. The reduction of band gap has an important impact on the transport properties. For instance, the transmission gap is decreased by about 48% and 16% in the transmission spectrum of the (5,5) and (8,0) heterojunctions, respectively. The current of the (5,5) heterojunction under small bias is almost doubled and the rectification ratio of the (8,0) heterojunction is enhanced by more than 120% due to SOI.

DOI: 10.1103/PhysRevB.91.205431 PACS number(s): 73.63.Fg, 73.22.−f, 71.70.Ej, 71.15.Mb

I. INTRODUCTION

The effect of spin-orbit interaction (SOI) plays the key role in spintronics. It holds promise for the generation, detection, and manipulation of spin currents, allowing coherent transmission of information within a device [1–4]. Its presence is also essential for the existence of topological insulators, a new state of matter [5–10]. SOI-induced spin transport effects have been studied extensively in two- and three-dimensional systems [11–15], while less attention has been paid to quasi-one-dimension such as carbon nanotubes presumably because of weak SOI for carbon-based material although the curvature of carbon nanotube can enhance SOI [16–18]. Comparing with carbon atoms, tungsten diselenide (WSe_2), which belongs to the family of transition-metal dichalcogenide (TMDC), is a compound of heavy atoms which has much larger SOI. It would be interesting to explore the SOI-induced transport properties through WSe_2 nanotubes and examine the related quantization effect along the transverse direction.

TMDC has been regarded as a promising candidate for field effect transistors (FETs) owing to its unique structural and electronic properties such as high mobility, organiclike flexibility, and larger on/off ratio [19–25]. Similar to graphite, TMDC crystallizes in a van der Walls layered structure where each layer consists of one sheet of transition-metal atoms sandwiched between two sheets of chalcogen atoms. Recent work shows that the explicit inversion symmetry breaking in monolayer TMDC allows the valley polarization by optical pumping with circularly polarized light [26]. Moreover, the giant spin-orbit interaction (SOI) originated from the d orbital of heavy-metal atoms has been proved to be important in the monolayer TMDC materials [27–29], which causes the energy splitting of the valence band maximum around the high-symmetry K point. The missing inversion symmetry also leads to a strong coupling between spin and valley degrees of freedom which opens an appealing prospect in potential applications of spintronics and valleytronics.

WSe_2, as a member of TMDC family, exhibits a bulk indirect band gap of 1.2 eV and the indirect-to-direct gap transition occurs when the thickness of WSe_2 reduces to a single monolayer, resulting in different photoluminescence efficiency [30–32]. A high intrinsic hole mobility up to 500 $cm^2/(Vs)$ has been observed in WSe_2 based FETs [33], which makes WSe_2 fascinating in device architecture for excellent transistors. Very recently, an interesting Zeeman-type spin polarization in WSe_2 under an external electric field with a systematic crossover from weak localization to weak antilocalization in magnetotransport arising from the significant SOI has been observed [34]. Although SOI plays such an important role in TMDC materials, there are still lacking in theoretical studies on their transport properties within SOI based on the density functional theory (DFT).

Analogous to carbon nanotubes, one-dimensional TMDC nanotubes have attracted much attention and prompted numerous studies. Theoretical study shows that zigzag and armchair MoS_2 nanotubes exhibit narrow direct and indirect band gaps, respectively [35]. Experimentally, WSe_2 nanotube has been successfully fabricated in experiments by the decomposition of ammonium selenometallates in a hydrogen atmosphere [36]. In this paper, employing the first-principles method combined with the nonequilibrium Green's function (NEGF), we study various transport properties through the single-wall WSe_2 nanotube heterojunctions with different chirality constructed by encapsulating with Au and Na atomic chains. The rectifying performance of the (8,0) heterojunction is investigated and large rectification ratio is found. For noise spectrum, the sub-Poissonian behavior is found for the (8,0) heterojunction with

*jianwang@hku.hk

 ©2015 American Physical Society

very small Fano factor under positive bias while Fano factor is nearly one showing Poissonian behavior under negative bias. For thermopower, we find that as one varies the Fermi energy, the thermopower can change its sign. Giant thermopower is found near the transmission gap of WSe_2 nanotubes. For dynamical conductance, we find that its imaginary part depends linearly on frequency with a negative slope showing capacitivelike behavior for the (5,5) heterojunction, while its real part exhibits nonlinear dependence on frequency. Our results show that the SOI affects the electronic-structure and transport properties of WSe_2 nanotubes significantly. The SOI decreases the transmission gap of the heterojunctions due to the reduction of the intrinsic band gap of both Au- and Na-doped WSe_2 nanotubes. The current of the (5,5) heterojunction is first enhanced by SOI under small biases and then saturates at almost the same value as that of the non-SOI case. We find that the rectification ratio of (8,0) heterojunction is significantly increased by SOI. Moreover, the real part of ac conductance of the (5,5) heterojunction is notably depressed by SOI.

We note that including SOI in the first-principles calculation can introduce huge computational burden. It not only doubles the matrix size for Green's function involved in the transport calculation, it also slows down the convergence rate in the self-consistent loop as well. For instance, even using a single-ζ polarized basis here, the matrix size of Green's function is close to 10 000 which is very large. Due to this reason, many first-principles transport investigations on nanodevices neglected the SOI without carefully studying the effect of SOI. One of the purposes of this investigation is to demonstrate that SOI should be included in the first-principles calculation both for band structure as well as for transport properties, especially for heavy atoms.

The paper is organized as follows. In Sec. II, we will first briefly introduce the prototype devices of WSe_2 nanotube and the NEGF-DFT method we used in this paper. In Sec. III, the numerical results of the Au- and Na-doped WSe_2 heterojunction, including the band structures, transmission coefficient, I-V characteristics, noise spectrum, thermopower, and dynamic conductance are presented. Finally, the discussion and conclusion are given in Sec. IV.

II. THEORETICAL FORMULAS AND COMPUTATIONAL METHOD

In this section, we will present theoretical formulas needed for various transport properties including I-V curve, noise spectrum, thermopower, dynamic conductance, and emittance. We then provide numerical methods for first-principles calculation.

A. Theoretical formalism

In general, the electric or heat current can be calculated using the Landauer-Büttiker formula ($e = \hbar = 1$)

$$I(V) = \int \frac{dE}{2\pi}(E - \mu - \mu_\alpha)^n [f_L - f_R]\mathcal{T}(E), \qquad (1)$$

where μ is the Fermi energy and $f_\alpha = 1/\{\exp[(E - \mu_\alpha)/k_B T_\alpha] + 1\}$ is the Fermi distribution function with μ_α the chemical potential, k_B the Boltzmann constant, and T_α the temperature of the α ($\alpha = L, R$) lead. $\mathcal{T}(E) = \mathrm{Tr}[\hat{\mathcal{T}}(E)]$ is the transmission coefficient with

$$\hat{\mathcal{T}}(E) = \Gamma_L G^r \Gamma_R G^a, \qquad (2)$$

where $\Gamma_{L,R} = i(\Sigma^r_{L,R} - \Sigma^a_{L,R})$ is the linewidth function with $\Sigma^{r(a)}$ being the retarded (advanced) self-energy of the leads and $G^{r(a)}$ is the retarded (advanced) Green's function. We emphasize that the transmission coefficient is bias dependent since the Hamiltonian contains Hartree potential that has to be solved from the Poisson equation with the boundary condition of applied bias. Equation (1) allows us to calculate both electric current ($n = 0$) and heat current ($n = 1$) due to the bias voltage as well as the temperature gradient. In addition, the Seebeck thermopower can also be calculated which is defined as the ratio between the voltage bias and the temperature gradient when there is no current in the device. In the linear-response regime (small bias voltage and small temperature gradient), it is given by [37]

$$S(\mu) = -\frac{1}{T}\frac{\mathcal{K}_1(\mu)}{\mathcal{K}_0(\mu)}, \qquad (3)$$

where

$$\mathcal{K}_n = \int dE[-\partial_E f(E)](E - \mu)^n \mathcal{T}(E), \qquad (4)$$

and T is the temperature of two electrodes.

Since the quantum transport is stochastic in nature, the current can fluctuate around its average [38]. It would be interesting to study the noise spectrum defined as [39]

$$\mathfrak{S} = \langle(\Delta I)^2\rangle = \int \frac{dE}{\pi}\{[f_L(1 - f_L) + f_R(1 - f_R)]\mathrm{Tr}[\hat{\mathcal{T}}] + (f_L - f_R)^2 \mathrm{Tr}[(1 - \hat{\mathcal{T}})\hat{\mathcal{T}}]\}, \qquad (5)$$

which will provide additional information about the current. We will study the noise spectrum at zero temperature. In this case, only the second term in Eq. (5) is nonzero. The Fano factor describing the magnitude of the electric fluctuation can be expressed as $F = \mathfrak{S}/2I$. One refers the noise spectrum Poissonian when $F = 1$. For $F > 1$, the system shows super-Poissonian behavior. This usually happens when I-V curve exhibits negative differential resistance (NDR) [40–42]. For $F < 1$, the system exhibits sub-Poissonian behavior.

In ac transport, it is known that the current consists of two parts: particle current and displacement current [43]. As the bias voltage is applied, the injected charge gives rise to the particle current while the displacement current is due to the induced charge as a result of the Coulomb interaction. For the dynamic conductance, a gauge-invariant and current-conserving theory have been formulated using the NEGF method [44]. When the bias voltage is sinusoidal, i.e., $v_\alpha \cos(\omega t)$, the dynamic conductance can be calculated from

$$G_{\alpha\beta}(\omega) = G^c_{\alpha\beta}(\omega) - G^d_\beta(\omega)\frac{\sum_\gamma G^c_{\alpha\gamma}(\omega)}{\sum_\gamma G^d_\gamma(\omega)}, \qquad (6)$$

where the subscripts α, β, and γ (L or R) label the leads. In the above equation, $G^c_{\alpha\beta}(\omega)$ represents the dynamic conductance

originated from the particle current defined as

$$G^c_{\alpha\beta}(\omega) = -\int \frac{dE}{2\pi}\frac{f-\bar{f}}{\omega}\mathrm{Tr}[-i(\bar{G}^r - G^a)\Gamma_\alpha\delta_{\alpha\beta} + \bar{G}^r\Gamma_\beta G^a\Gamma_\alpha], \quad (7)$$

with $\bar{G}^r = G^r(E+\omega)$ and $\bar{f} = f(E+\omega)$. While $G^d_\beta(\omega)$ is the contribution from the displacement current given by [44]

$$G^d_\beta(\omega) = -i\int \frac{dE}{2\pi}\mathrm{Tr}[\bar{G}^r\Gamma_\beta G^a(f-\bar{f})]. \quad (8)$$

In the low-frequency limit, the dynamic conductance has the following expansion [45]:

$$G_{\alpha\beta}(\omega) = G_{\alpha\beta}(0) - i\omega E_{\alpha\beta} + \omega^2 K_{\alpha\beta} + O(\omega^3), \quad (9)$$

where $G_{\alpha\beta}(0)$ is the dc conductance, $E_{\alpha\beta}$ is the so-called emittance which describes the low-frequency response of the system, namely, the phase difference between the current and voltage, and $K_{\alpha\beta}$ describes the low-frequency dynamic dissipation. From the above definition of the dynamic conductance, the emittance can be expressed as [46]

$$E_{\alpha\beta} = E^c_{\alpha\beta} - \frac{\mathrm{Tr}[dn_\alpha/dE]\mathrm{Tr}[dn_\beta/dE]}{\mathrm{Tr}[dn/dE]}, \quad (10)$$

where $E^c_{\alpha\beta}$ is the emittance contributed from the particle current

$$E^c_{\alpha\beta} = \mathrm{Tr}\left[\frac{dn_{\alpha\beta}}{dE}\right], \quad (11)$$

with $dn_{\alpha\beta}/dE$ the partial density of states (DOS) defined as

$$\frac{dn_{\alpha\beta}}{dE} = \frac{1}{2\pi}\mathrm{Re}(\delta_{\alpha\beta}G^r\Gamma_\alpha G^r + iG^r\Gamma_\beta G^a\Gamma_a G^r). \quad (12)$$

The injectivity $dn_\alpha/dE = \sum_\beta dn_{\alpha\beta}/dE$ describes the local density of states (LDOS) when an incoming electron is injected from the electrode α and the total LDOS $dn/dE = \sum_\alpha dn_\alpha/dE$. From Eq. (10), we see that the second term is positive definite since it consists of DOS. Note that Eq. (11) can be rewritten in terms of scattering matrix as [45]

$$E^c_{\alpha\beta} = \int \frac{dE}{4\pi i}\left(-\frac{df}{dE}\right)\mathrm{Tr}\left[s^\dagger_{\alpha\beta}\frac{ds_{\alpha\beta}}{dE} - \frac{ds^\dagger_{\alpha\beta}}{dE}s_{\alpha\beta}\right]. \quad (13)$$

Depending on the sign of emittance E_{LL}, two different responses can be obtained. For a capacitor, there is no transmission and $s_{LR} = 0$ ($E^c_{LR} = 0$), hence, $E_{LR} < 0$ from From Eq. (10). For an inductor, there is no reflection hence we have $s_{LL} = 0$ ($E^c_{LL} = 0$) and $E_{LL} < 0$. On the other hand, since the theory is gauge invariant, $E_{LL} + E_{LR} = 0$. We finally have the following: if $E_{LL} > 0$ the response is capacitivelike (voltage lags behind current) while for $E_{LL} < 0$ it is an inductivelike response.

B. Numerical procedure

Now, we discuss the procedure for numerical calculation. For the two-probe device we considered, one Au or Na atom is encapsulated into the center of a unit cell of the single-wall WSe_2 nanotube. Then, Au- (Na-) doped unit cell is repeated forming left (right) semi-infinite electrode to connect the central scattering region, as shown in Fig. 1. To account for the effect of chirality, we choose the typical (5,5) armchair and (8,0) zigzag WSe_2 nanotube, which are indirect and direct band-gap semiconductors, respectively. The central region of the (5,5) and (8,0) WSe_2 nanotube systems is about 20.16 and 21.76 Å, respectively.

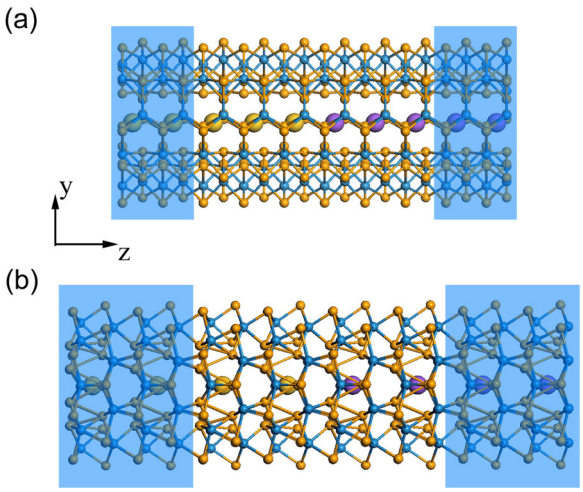

FIG. 1. (Color online) Schematic diagram of (a) (5,5) and (b) (8,0) WSe_2 nanotube heterojunctions encapsulated with Au and Na atomic chains. The light blue shadows represent the electrodes. The sky blue, dark yellow, golden, and purple balls denote the tungsten, selenium, gold, and sodium atoms, respectively.

The calculation of electronic and quantum transport properties is carried out using the first-principles method within the nonequilibrium Green's function, as implemented in the NANODCAL package [47,48]. The exchange and correlation functional is approximated by generalized gradient approximation (GGA) with Perdew-Burke-Ernzerhof (PBE) [49] functional and the standard norm-conserving pseudopotential is used to describe the atomic cores [50]. The energy cutoff of the real-space grid and the convergence criteria of the Hamiltonian and density matrix are taken as 4000 and 10^{-5} eV, respectively. The Brillouin zone is sampled by $1 \times 1 \times 100$ grids for calculations of both leads.

The basis set used in our calculation is optimized by fitting the band structures with and without SOI obtained from the electronic calculation using Vienna *ab initio* simulation package (VASP) [51,52], in which $1 \times 1 \times 12$ gamma centered Monkhorst-Pack grids are sampled for the self-consistent field calculation. We find excellent agreement for band structures of the (5,5) and (8,0) WSe_2 nanotubes within and without SOI calculated by VASP and NANODCAL using a single-ζ polarized linear combination of atomic orbital (LCAO) basis. Therefore, a single-ζ polarized basis is good enough to describe the WSe_2 nanotube system.

In order to consider the SOI, the Kohn-Sham Hamiltonian is expressed by the kinetic energy $\mathbf{T}$, Hartree potential $\mathbf{V}_H$, exchange and correlation potential $\mathbf{V}_{xc}$, scalar relativistic $\mathbf{V}_{sc}$, and spin-orbital $\mathbf{V}_{so}$ potentials as [53]

$$\mathbf{H} = \mathbf{T} + \mathbf{V}_H + \mathbf{V}_{xc} + \mathbf{V}_{sc} + \mathbf{V}_{so}, \quad (14)$$

with

$$\mathbf{V}_{sc}+\mathbf{V}_{so}=\sum_{l,m}\left[V_l\mathbb{1}_\sigma+V_l^{so}\vec{L}\cdot\vec{S}\right]|l,m\rangle\langle l,m|, \quad (15)$$

where $\mathbb{1}_\sigma$ is the unit operator in spin space and $|l,m\rangle$ presents the regular angular momentum states. In the LCAO scheme, the eigenstates of the Kohn-Sham Hamiltonian are expanded by a set of localized orbitals $|\phi_i\rangle$, therefore, the onsite spin-orbit term can be calculated by

$$V_{ij}^{so}=\langle\phi_i|\mathbf{V}_{so}|\phi_j\rangle. \quad (16)$$

Since the above Hamiltonian is a 2×2 matrix in the spin space, the corresponding retarded Green's function of the system should be defined within the noncollinear spin space as

$$G^r=\begin{pmatrix}G^r_{\uparrow\uparrow} & G^r_{\uparrow\downarrow}\\ G^r_{\downarrow\uparrow} & G^r_{\downarrow\downarrow}\end{pmatrix}. \quad (17)$$

III. NUMERICAL RESULTS

In this section, we will calculate the band structures of Au- and Na-encapsulated (5,5) and (8,0) WSe_2 nanotubes and various transport properties of WSe_2 nanotube heterojunction with and without SOI including transmission coefficient, I-V characteristics, noise spectrum, thermopower, and dynamic conductance.

A. Electronic properties

Figure 2 depicts the band structures of Au- and Na-doped WSe_2 nanotubes. From Fig. 2(a) we see that the (5,5) WSe_2 nanotube with Au atoms exhibits n-type semiconducting characteristics with an indirect band gap of 125 meV without SOI. It decreases by 58% and becomes to 52 meV after considering the SOI. Similarly, Fig. 2(b) shows that when we replace the donor by Na atoms, the intrinsic indirect band gap of the system is about 156 meV without SOI. When the SOI is introduced, the intrinsic band gap of Na-doped WSe_2 nanotube vanishes.

The band structure of Au-doped (8,0) WSe_2 nanotube is plotted in Fig. 2(c), which exhibits p-type semiconducting characteristics. After introducing the SOI, the intrinsic direct band gap decreases from 304 to 190 meV with a strong splitting of the bottom of conduction band. We find that Na atoms behave like n-type dopants in the (8,0) WSe_2 nanotube from its band structures in Fig. 2(d). Its intrinsic band gap reduces from 288 to 167 meV when including the SOI. The decrease of nearly 40% in the intrinsic band gap indicates that SOI makes a significant contribution in the electronic properties of Au- (Na-) doped WSe_2 nanotubes.

B. Transmission coefficient

The transmission spectrum of Au- and Na-doped WSe_2 nanotube heterojunctions is calculated based on the NEGF-DFT scheme as shown in Fig. 3. Here, the transmission coefficients with SOI are scaled down by half in order to compare with those without SOI. As for the (5,5) heterojunction, due to the n-type semiconducting properties for both Au- and Na-doped (5,5) WSe nanotubes, the heterojunction exhibits metallic characteristics, with a transmission coefficient about 0.37 at the Fermi level in the absence of SOI which decreases to about 0.24 when the SOI is included, namely, the effect of SOI reduces the transmission coefficient at the Fermi level by about 35%. We note that there is a transmission gap of 0.37 eV below the Fermi level for system without SOI which reduces to only half (0.18 eV) after introducing the SOI, originating from the intrinsic band gap of the doped nanotube.

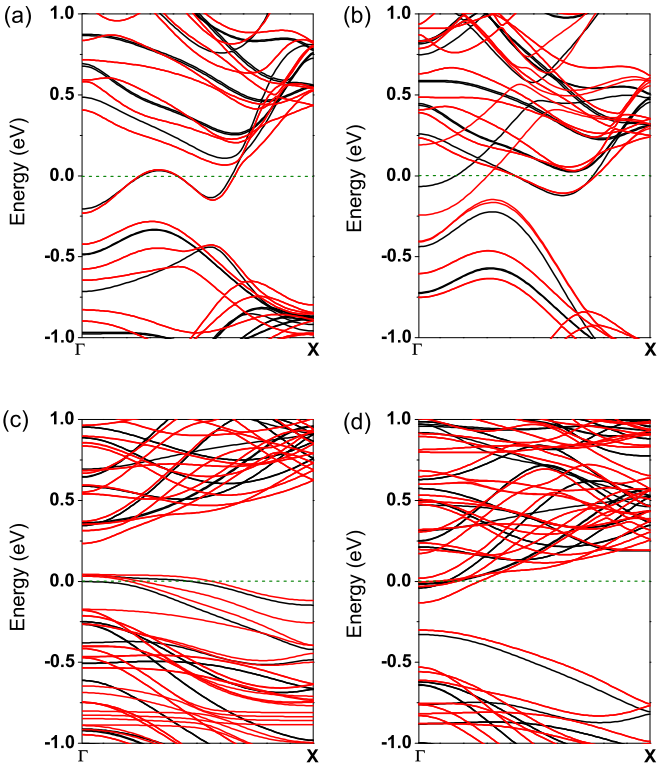

FIG. 2. (Color online) Band structures without SOI (black solid line) and with SOI (red dashed line) of (a) Au-doped (5,5) WSe_2 nanotube, (b) Na-doped (5,5) WSe_2 nanotube, (c) Au-doped (8,0) WSe_2 nanotube, and (d) Na-doped (8,0) WSe_2 nanotube.

For the (8,0) heterojunction, since Au and Na atoms play different roles in the WSe_2 nanotube, namely, behaving like the p- and n-type dopants, respectively, the transmission spectrum possesses a large transmission gap of 0.66 eV without SOI, as shown in Fig. 3(b). This transmission gap reduces by about 16% and becomes 0.55 eV when the SOI is introduced. We also find that the transmission coefficients for the highest occupied molecular orbital (HOMO) and the lowest unoccupied molecular orbital (LUMO) are slightly decreased by SOI for both (5,5) and (8,0) heterojunctions.

C. I-V characteristics

To further study the effect of SOI on the transport properties, the I-V characteristics of WSe_2 nanotube heterojunctions are calculated as shown in Fig. 4. The current of (5,5) heterojunction without considering SOI first increases rapidly under the positive bias and then saturates at 24.5 μA with the bias of 0.3 V, while the current under the negative bias decreases slowly with oscillations. Once the bias exceeds 0.4 V, the current decreases as the increasing of the applied voltage, which exhibits the NDR effect. After introducing the SOI,

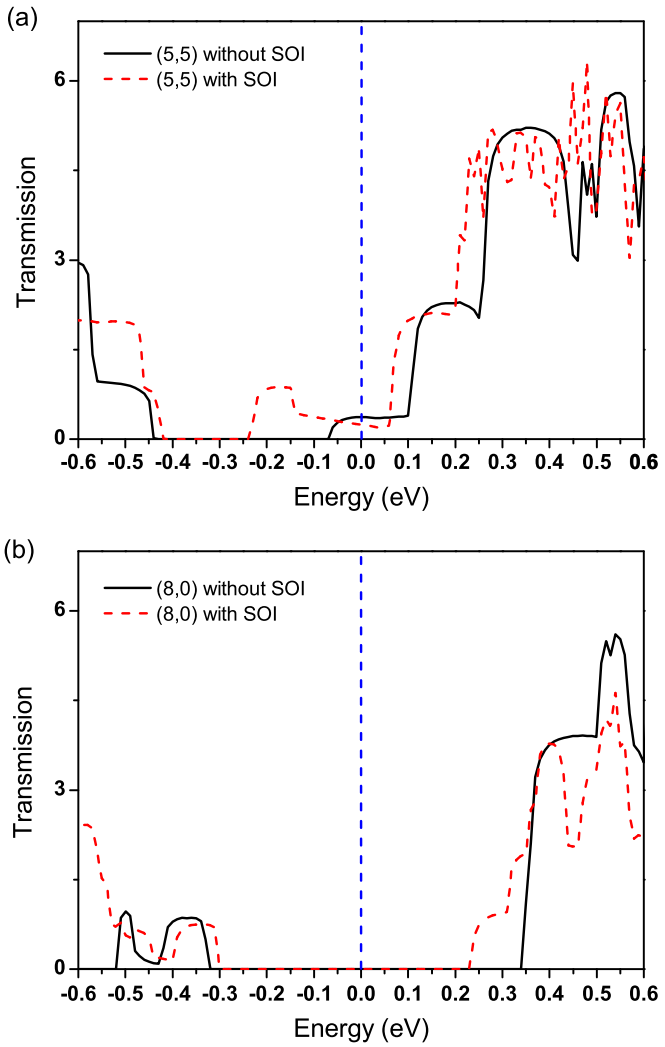

FIG. 3. (Color online) Transmission coefficients of (a) (5,5) and (b) (8,0) WSe_2 nanotube heterojunction.

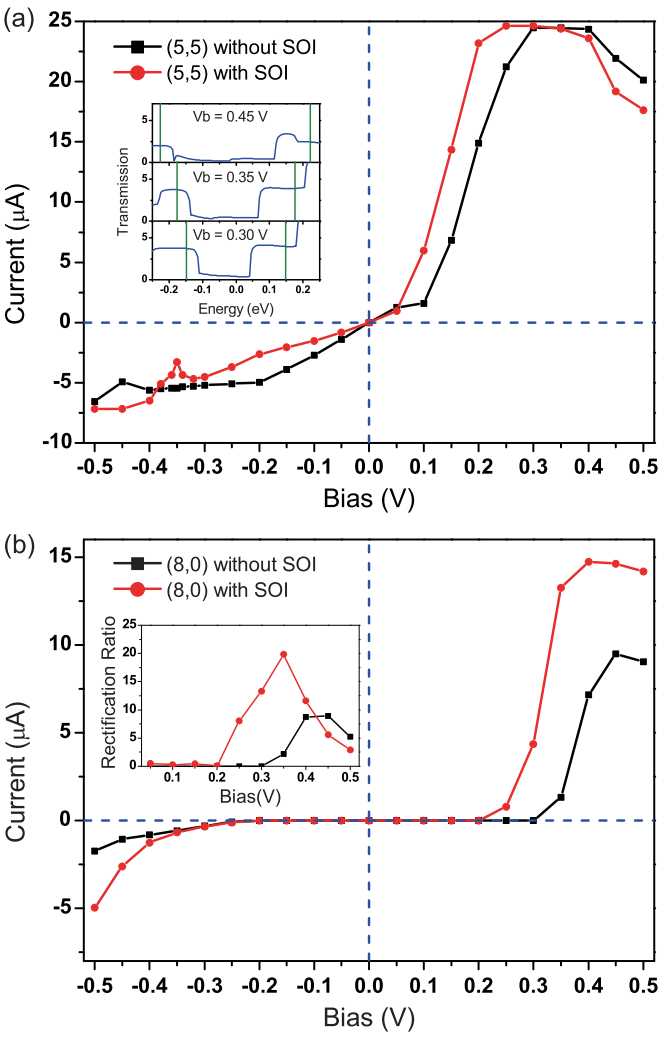

FIG. 4. (Color online) (a) I-V characteristics of (5,5) WSe_2 nanotube heterojunction. Inset: transmission spectrum of (5,5) WSe_2 nanotube heterojunction under a bias of 0.3 V (top panel), 0.35 V (middle panel), and 0.45 V (bottom panel). The green lines denote the bias window. (b) I-V characteristics of (8,0) WSe_2 nanotube heterojunction. Inset: rectification ratio as a function of applied bias of (8,0) WSe_2 nanotube heterojunction.

the current with positive bias enhances significantly before the saturation while it increases slightly for the negative bias larger than -0.35 V. The saturation voltage decreases to about 0.25 V with almost the same saturation current of 24.6 μA compared with that of the non-SOI case. The NDR effect also occurs once the bias exceeds 0.35 eV. To explain the NDR effect, the bias-dependent transmission spectrum with SOI is presented in the inset of Fig. 4(a). We find that under a bias of 0.3 V, the transmission gap of the system shifted to the higher energy and reduces to about 0.15 eV compared with that of the equilibrium case as plotted in Fig. 3. When the bias increases from 0.3 to 0.35 V, although the transmission gap increases to about 0.20 eV, the integration area of transmission coefficient does not change much due to the broadening of bias window, leading to almost the same current. After the bias increases to 0.45 V, we find that the transmission gap is notably increased to about 0.30 eV. Due to the significant suppression of transmission coefficient contributed by HOMO and unoccupied molecular orbital at about 0.2 eV, the current then decreases compared with that under the bias of 0.35 V, resulting in the NDR effect in the (5,5) heterojunction.

The I-V curves of the (8,0) WSe_2 nanotube heterojunction shown in Fig. 4(b) exhibit the typical characteristics of a p-n junction. The system shows a threshold voltage of 0.35 V without SOI under the positive bias. After considering the SOI, it decreases by about 0.1 V and the corresponding on-current increases. However, both the threshold voltage and on-current keep the same under the negative bias regardless of the SOI. Moreover, once the device turns on, the current under the positive bias is much larger than that under the negative bias. Therefore, to fully evaluate the rectifying performance of the junction, we define a rectification ratio as a function of the applied bias $R(V) = |\frac{I(+V)}{I(-V)}|$, as shown in the inset of Fig. 4(b). We find that the rectification ratio approaches 9 for the non-SOI system in the bias region between 0.4 and 0.45 V. Once the SOI is included, the maximum rectification ratio significantly enhances by more than 120% and approaches to 20 at the

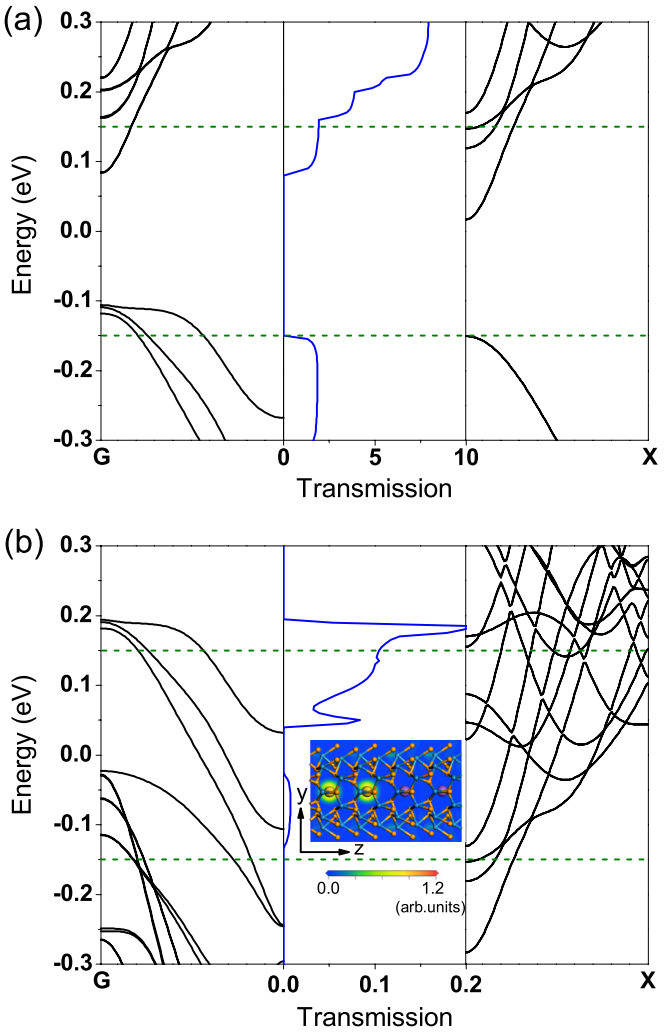

FIG. 5. (Color online) Band structure of the left lead (left panel), transmission spectrum (middle panel), and band structure of the right lead (right panel) for the (8,0) WSe_2 nanotube heterojunction under a bias of (a) 0.3 V and (b) −0.3 V. Inset: real-space distribution of LDOS for (8,0) heterojunction at −0.05 eV under a bias of −0.3 V. The green dotted lines indicate the bias window.

bias of 0.35 V. The high rectification ratio shows potential applications in the design of diodes and switches.

To further understand the rectifying performance, the band structures of left and right leads under the bias of ±0.3 V with the corresponding transmission spectrum are plotted in Fig. 5. Due to the positive bias, the bottom of the conductance band of the left lead is shifted into the bias window while part of the conductance band of the right lead also remains in this energy region. Therefore, a transmission plateau of 1.8 occurs around 0.1 eV, which contributes to the relatively large current of about 4.36 μA. In contrast, although part of the valence band of the left lead remains in the bias window, the top of the valence band of the right lead is still outside of the bias window because the applied bias is not large enough. Hence, the valence bands of the system do not contribute to the current for the positive bias less than 0.3 V. For the case under a bias of −0.3 V, we find the energy bands of left lead in the bias window mainly originated from Au atoms, while the energy bands of the right lead in energy region of [0.05, 0.15] eV are partly contributed by Na atoms. Therefore, electron transport between the metallic chain occurs but is weak due to the large intervals. The energy bands of the right lead in the rest region of the bias window are mainly originated from W atoms so that the transmission coefficient almost vanishes in this energy region. Moreover, we analyze the LDOS in the real space of the heterojunction during this energy region. The inset of Fig. 5(b) presents the LDOS at −0.05 eV as an example and it shows that the LDOS is mainly localized on Au atoms resulting in the extremely small transmission coefficient which agrees with our band analysis. Consequently, although both the valence bands of left lead and the conductance bands of right lead are shifted into the bias window, the corresponding transmission coefficients are very small, which causes the tiny current at −0.3 V and further leads to the high rectification ratio.

D. Noise spectrum

The noise spectrum describing the current fluctuation is studied for the (5,5) WSe_2 nanotube heterojunction which is plotted in Fig. 6(a). We find that the noises with and without

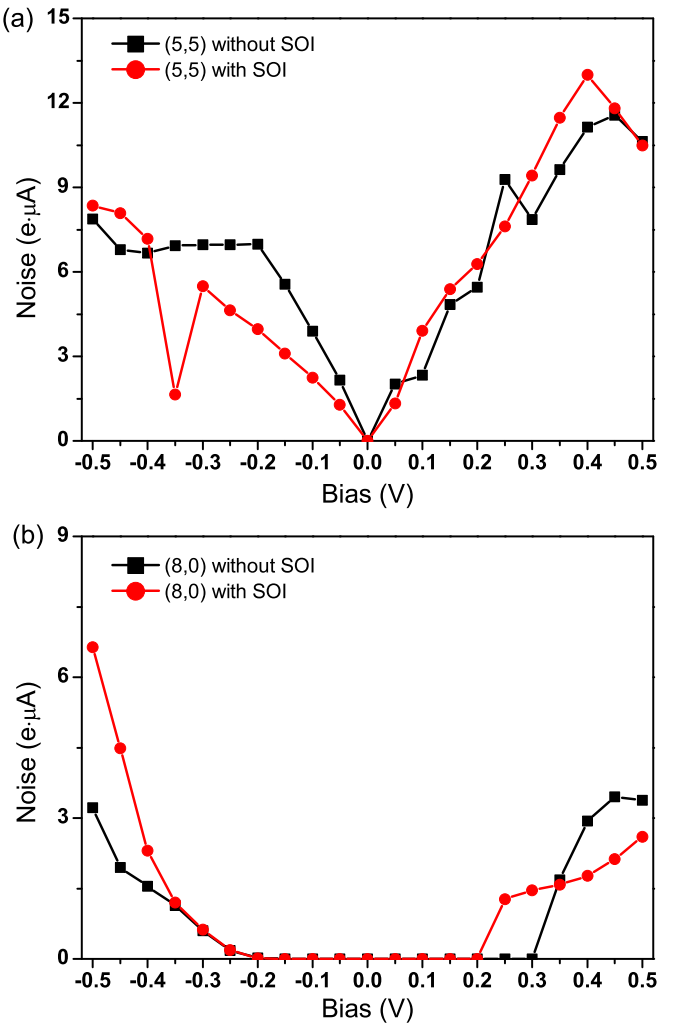

FIG. 6. (Color online) Noise spectrum of (a) (5,5) and (b) (8,0) WSe_2 nanotube heterojunctions as a function of applied bias.

SOI show almost linear characteristics under positive bias and behave similarly when the bias is lesser than 0.2 V. Once the applied bias reaches 0.3 V, the noises with SOI become a little bit larger than those without SOI. For the negative bias, the noise spectrum with and without SOI also increases linearly first with the decreasing applied bias. The noise without SOI is about 70% higher than that with SOI for the small bias larger than −0.2 V while it becomes lower than those with SOI when the bias lesser than −0.4 V. Moreover, a flat region of the noise spectrum is found in the bias region of [−0.45, − 0.2] V due to the almost unchanged current as shown in Fig. 4(a).

Figure 6(b) presents the noise spectrum of the (8,0) WSe_2 nanotube heterojunction as a function of applied bias. We find that there is a gap in the noise spectrum since the system has not turned on, which agrees with the corresponding current as shown in Fig. 4(b). Once the device turns on at the positive bias, the noise with SOI is close to that without SOI under the bias of 0.35 V and then becomes about 40% lesser than that without SOI under other biases. For the negative bias, the noises with SOI are larger than those without SOI after the device turns on and are almost double than those without SOI once the applied bias exceeds −0.35 V.

To further study the electric current fluctuation, we also calculate the Fano factor of the WSe_2 nanotube heterojunction. Figure 7 shows the Fano factor of the (8,0) WSe_2 nanotube heterojunction as an example with different bias under which the device has been turned on. We find that the Fano factor is very small for positive bias showing sub-Poissonian behavior. Under the negative bias, the Fano factor is close to one showing Poissonian behavior. We can understand these behaviors as follows. To analyze the noise spectrum, we diagonalize the voltage-dependent transmission matrix $\hat{\mathcal{T}}$ with eigenvalue $\mathcal{T}_i$ characterizing the transmission coefficient for the corresponding transmission channel. The shot noise can be written as

$$\mathcal{S} = \int \frac{dE}{\pi}(f_L - f_R)^2 \sum_i [(1-\mathcal{T}_i)\mathcal{T}_i]. \tag{18}$$

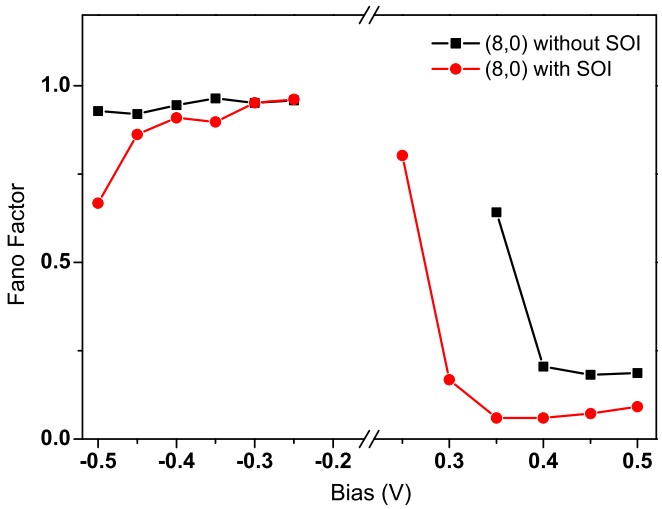

FIG. 7. (Color online) Fano factor of (8,0) WSe_2 nanotube heterojunction as a function of applied bias.

For positive bias (except close to the transmission gap), our analysis shows that the transport of each transmission channel of the system is nearly ballistic with $\mathcal{T}_i$ close to one. Therefore, the shot noise $\mathcal{S}$ is very small proportional to $\int_{\mu_L}^{\mu_R} dE \sum_i (1-\mathcal{T}_i)$, while current is large proportional to $\int_{\mu_L}^{\mu_R} dE \sum_i \mathcal{T}_i$. This gives rise to very small Fano factor. At negative bias, the transmission coefficient for each transmission channel is close to 0 especially near the transmission gap. As a result, the shot noise $\mathcal{S}$ is again very small proportional to $\int_{\mu_L}^{\mu_R} dE \sum_i \mathcal{T}_i$ while the current is also small proportional to $\int_{\mu_L}^{\mu_R} dE \sum_i \mathcal{T}_i$. Because of this, the system shows a Poissonian behavior. Moreover, the effect of SOI on shot noise is clearly seen from the figure. It is worth noting that despite the NDR effect under the bias of 0.5 V without SOI, the Fano factor does not exhibit super-Poissonian behavior as observed in experiments. We emphasize that due to the mean field approximation, the super-Poissonian behavior in NDR region can not be obtained from the general DFT frame. It has been shown in Ref. [42] that if the correlation of Coulomb interaction is included the Fano factor changes from sub-Poissonian to super-Poissonian in the NDR region.

E. Seebeck thermopower

We then calculate the Seebeck thermopower as a function of the Fermi level for the (5,5) and (8,0) WSe_2 nanotube heterojunctions for a fixed temperature of 20 K and the results are shown in Fig. 8. The following observations are in order. (1) The thermopower can change its sign when the Fermi level is varied which can be achieved by applying a gate voltage in the scattering region. (2) Giant thermopower is found when Fermi level is close to the transmission gap. We note that a giant thermopower of $S = 100\ \mu$V/K is found experimentally in carbon nanotube in the Kondo regime [54]. (3) The effect of SOI is to shift the peaks of thermopower.

In order to understand these behaviors of thermopower, we expand the transmission coefficient $\mathcal{T}$ in $\mathcal{K}_1(\mu)$ in Eq. (4) around μ at low temperatures so that the thermopower in Eq. (3) can be expressed as

$$S(\mu) = -\frac{k_B^2 \pi^2 T}{3} \frac{\frac{d\mathcal{T}(E)}{dE}\big|_{\epsilon=\mu}}{\mathcal{T}(\mu)}. \tag{19}$$

We see that the Seebeck thermopower is proportional to the energy derivative of the logarithm of the transmission coefficient. Here, large thermopower requires large $d\mathcal{T}/dE$ and small $\mathcal{T}$. Therefore, the thermopower with SOI for the (5,5) WSe_2 nanotube heterojunction is relatively small at the positive energy region (when $\mu > 0.1$ eV) because of the large transmission coefficient. Near $\mu = 0.06$ eV, $d\mathcal{T}/dE$ is very large and $\mathcal{T}$ is smaller, resulting a giant thermopower $S = 227\ \mu$V/K. The large peak and valley at negative bias occur near the transmission gap with large $d\mathcal{T}/dE$ and very small $\mathcal{T}$ giving rise to giant thermopower $S \approx 1000\ \mu$V/K. Once the SOI is turned off, due to the increase of the transmission gap below the Fermi energy, the thermopower valley mentioned above shifts to the energy of 0.11 eV and the thermopower peak shifted from −0.41 to −0.42 eV. Similarly, as for the (8,0) WSe_2 nanotube heterojunction, the large thermopower peak and valley with SOI locate at −0.27 and 0.21 eV corresponding

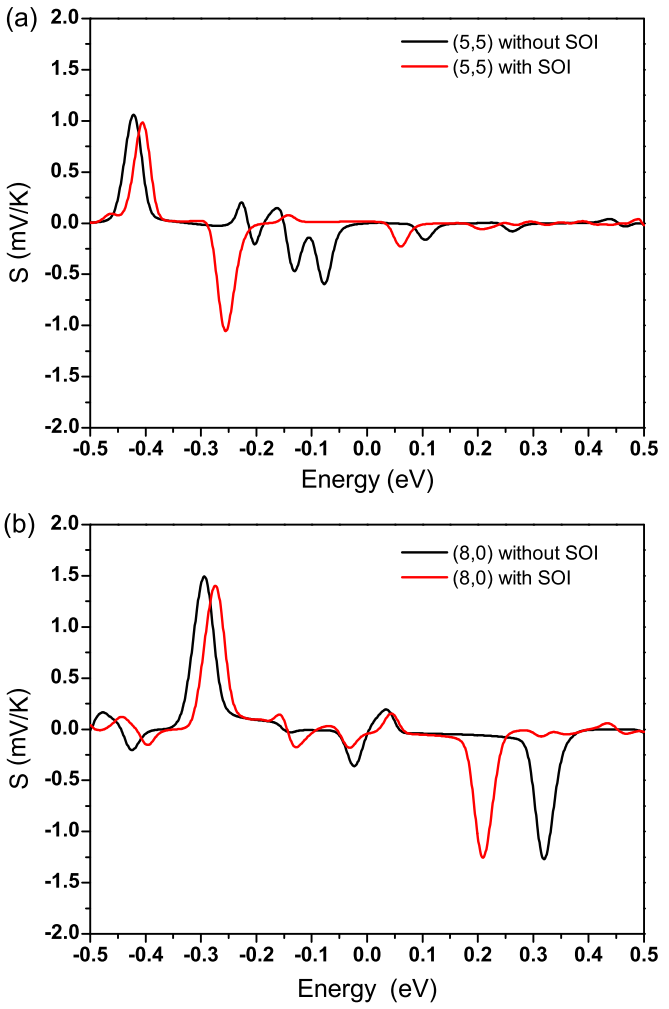

FIG. 8. (Color online) Thermopower of (a) (5,5) and (b) (8,0) WSe_2 nanotube heterojunctions as a function of the Fermi level under a fixed temperature of 20 K.

near the edge of large transmission gap, which shift to −0.30 and 0.32 eV after switching off the SOI, respectively.

F. Dynamic conductance and emittance

To study the dynamic conductance behavior, we choose the metallic (5,5) WSe_2 nanotube heterojunction and calculate its ac conductance. Figure 9 presents the real part of dynamic conductance G_{LL} of the (5,5) WSe_2 nanotube heterojunction versus frequency and the corresponding imaginary part of G_{LL} is plotted in the inset. We find that the imaginary part and real part of ac conductance exhibit linear and nonlinear dependency on frequency, respectively. Specifically, when the frequency increases from zero, the real part of G_{LL} decreases quickly at first, reaches the minimum at 5.5 THz, and then increases slowly. For the imaginary part of G_{LL}, linear dependence on frequency shows that the emittance dominates the imaginary part of ac conductance. The negative sign indicates the capacitivelike behavior. This is consistent with the small transmission coefficient near the Fermi level shown in Fig. 3(a), which is originated from the heterojunction doped by Au and Na atoms.

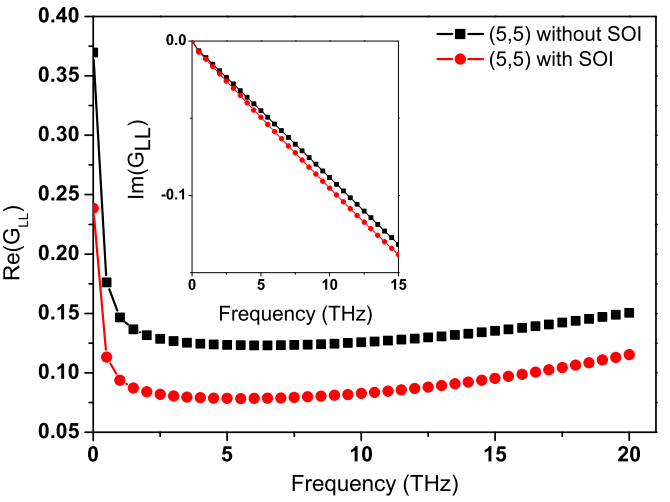

FIG. 9. (Color online) Real part of dynamic conductance G_{LL} of (5,5) WSe_2 nanotube heterojunction as a function of frequency. Inset: imaginary part of dynamic conductance G_{LL} of (5,5) WSe_2 nanotube heterojunction as a function of frequency.

The emittance as a function of the chemical potential is also calculated for the (5,5) WSe_2 nanotube heterojunction and E_{LL} is plotted in Fig. 10. We find that the emittance E_{LL} with SOI is almost independent of the chemical potential under negative chemical potential. While for the positive chemical potential, the emittance drops quadratically and then becomes independent of the chemical potential again, owing to the fact that the corresponding number of subband of the left lead decreases from three to only one, as shown in the inset of Fig. 10. If the SOI is turned off, we have similar behaviors for real and imaginary parts of G_{LL} except that emittance with SOI is smaller than that without SOI. The emittance E_{LL} without SOI is a little bit different. It decreases quadratically when the Fermi level changes towards higher energies and then remains

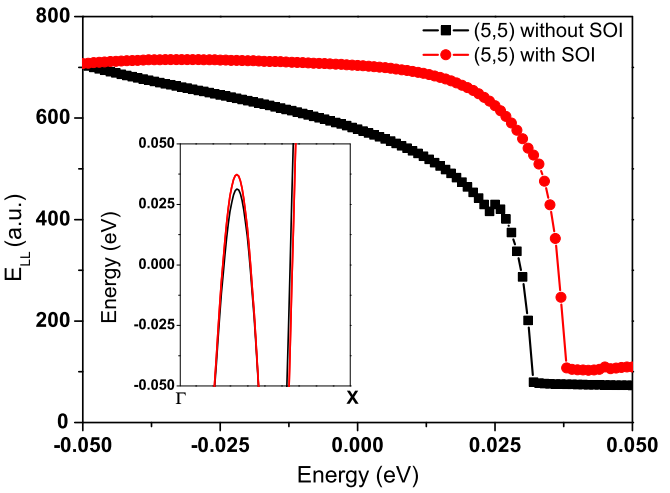

FIG. 10. (Color online) Emittance E_{LL} of (5,5) WSe_2 nanotube heterojunction as a function of chemical potential. Inset: band structures without SOI (black line) and with SOI (red line) for the left lead of (5,5) heterojunction, i.e., Au-doped (5,5) WSe_2 nanotube.

almost the same when the chemical potential is larger than 0.03 eV due to the decrease of subbands of the left lead.

IV. CONCLUSION

In summary, we have used a first-principles calculation combined with the NEGF method to study various transport properties including I-V curves, noise spectrum, thermopower, and dynamical conductance of WSe_2 nanotube heterojunctions. For I-V curves, we investigate the rectifying performance for the (8,0) WSe_2 nanotube heterojunction which shows a large rectification ratio. For shot noise spectrum, the (8,0) heterojunction exhibits sub-Poissonian and Poissonian behavior under positive and negative bias, respectively. For thermopower, we find that the thermopower can change its sign when the Fermi level is varied and a giant thermopower is found near the transmission gap. For dynamical conductance, we find that its imaginary part depends linearly on frequency exhibiting capacitivelike behavior for the (5,5) heterojunction while its real part shows nonlinear dependence on frequency.

Our results also show that the SOI effect plays an important role on the electronic-structure and transport properties of WSe_2 nanotubes. The transmission gap of WSe_2 nanotube heterojunctions is significantly decreased by SOI due to the reduction of the intrinsic band gap of both Au- and Na-doped WSe_2 nanotubes. The current of the (5,5) heterojunction under small bias is notably enhanced by SOI and the rectification ratio of the (8,0) heterojunction is increased by more than 120% due to SOI. Moreover, the real part of ac conductance of (5,5) heterojunction is depressed by SOI while the corresponding emittance is enhanced.

ACKNOWLEDGMENTS

The authors would like to thank Y. H. Zhao for much useful help concerning the basis optimization. This work was financially supported by the Research Grant Council (Grant No. HKU 705212P), the University Grant Council (Contract No. AoE/P-04/08) of the Government of HKSAR, and the National Natural Science Foundation of China (Grant No. 11374246).

[1] S. A. Wolf, D. D. Awschalom, R. A. Buhrman, J. M. Daughton, S. von Molnár, M. L. Roukes, A. Y. Chtchelkanova, and D. M. Treger, Science **294**, 1488 (2001).
[2] J. M. Kikkawa and D. D. Awschalom, Nature (London) **397**, 139 (1999).
[3] Y. Ohno, D. K. Young, B. Beschoten, F. Matsukura, H. Ohno, and D. D. Awschalom, Nature (London) **402**, 790 (1999).
[4] R. Fiederling, M. Keim, G. Reuscher, W. Ossau, G. Schmidt, A. Waag, and L. W. Molenkamp, Nature (London) **402**, 787 (1999).
[5] C. L. Kane and E. J. Mele, Phys. Rev. Lett. **95**, 146802 (2005).
[6] B. A. Bernevig, T. L. Hughes, and S.-C. Zhang, Science **314**, 1757 (2006).
[7] M. Z. Hasan and C. L. Kane, Rev. Mod. Phys. **82**, 3045 (2010).
[8] J. E. Moore, Nature (London) **464**, 194 (2010).
[9] X.-L. Qi and S.-C. Zhang, Phys. Today **63**(1), 33 (2010).
[10] X.-L. Qi and S.-C. Zhang, Rev. Mod. Phys. **83**, 1057 (2011).
[11] Y. K. Kato, R. C. Myers, A. C. Gossard, and D. D. Awschalom, Science **306**, 1910 (2004).
[12] M. König, S. Wiedmann, C. Brüne, A. Roth, H. Buhmann, L. W. Molenkamp, X.-L. Qi, and S.-C. Zhang, Science **318**, 766 (2007).
[13] S. M. Frolov, S. Luscher, W. Yu, Y. Ren, J. A. Folk, and W. Wegscheider, Nature (London) **458**, 868 (2009).
[14] Y. L. Chen, J. G. Analytis, J.-H. Chu, Z. K. Liu, S.-K. Mo, X. L. Qi, H. J. Zhang, D. H. Lu, X. Dai, Z. Fang, S. C. Zhang, I. R. Fisher, Z. Hussain, and Z.-X. Shen, Science **325**, 178 (2009).
[15] Y. Xia, D. Qian, D. Hsieh, L. Wray, A. Pal, H. Lin, A. Bansil, D. Grauer, Y. S. Hor, R. J. Cava, and M. Z. Hasan, Nat. Phys. **5**, 398 (2009).
[16] F. Kuemmeth, S. Ilani, D. C. Ralph, and P. L. McEuen, Nature (London) **452**, 448 (2008).
[17] T. S. Jespersen, K. Grove-Rasmussen, J. Paaske, K. Muraki, T. Fujisawa, J. Nygard, and K. Flensberg, Nat. Phys. **7**, 348 (2011).
[18] G. Steele, F. Pei, E. Laird, J. Jol, H. Meerwaldt, and L. Kouwenhoven, Nat. Commun. **4**, 1573 (2013).
[19] B. Radisavljevic, A. Radenovic, J. Brivio, V. Giacometti, and A. Kis, Nat. Nanotechnol. **6**, 147 (2011).
[20] S. Kim, A. Konar, W.-S. Hwang, J. H. Lee, J. Lee, J. Yang, C. Jung, H. Kim, J.-B. Yoo, J.-Y. Choi, Y. W. Jin, S. Y. Lee, D. Jena, W. Choi, and K. Kim, Nat. Commun. **3**, 1011 (2012).
[21] H. Fang, S. Chuang, T. C. Chang, K. Takei, T. Takahashi, and A. Javey, Nano Lett. **12**, 3788 (2012).
[22] Y. Zhang, J. Ye, Y. Matsuhashi, and Y. Iwasa, Nano Lett. **12**, 1136 (2012).
[23] H. S. Shin, G. Eda, L.-J. Li, K. P. Loh, and H. Zhang, Nat. Chem. **5**, 263 (2013).
[24] W. Liu, J. Kang, D. Sarkar, Y. Khatami, D. Jena, and K. Banerjee, Nano Lett. **13**, 1983 (2013).
[25] J.-K. Huang, J. Pu, C.-L. Hsu, M.-H. Chiu, Z.-Y. Juang, Y.-H. Chang, W.-H. Chang, Y. Iwasa, T. Takenobu, and L.-J. Li, ACS Nano **8**, 923 (2014).
[26] H. Zeng, J. Dai, W. Yao, D. Xiao, and X. Cui, Nat. Nanotechnol. **7**, 490 (2012).
[27] Z. Y. Zhu, Y. C. Cheng, and U. Schwingenschlögl, Phys. Rev. B **84**, 153402 (2011).
[28] D. Xiao, G.-B. Liu, W. Feng, X. Xu, and W. Yao, Phys. Rev. Lett. **108**, 196802 (2012).
[29] T. Cao, G. Wang, W. Han, H. Ye, C. Zhu, J. Shi, Q. Niu, P. Tan, E. Wang, B. Liu, and J. Feng, Nat. Commun. **3**, 887 (2012).
[30] L. C. Upadhyayula, J. J. Loferski, A. Wold, W. Giriat, and R. Kershaw, J. Appl. Phys. **39**, 4736 (1968).
[31] Q. H. Wang, K. Kalantar-Zadeh, A. Kis, J. N. Coleman, and M. S. Strano, Nat. Nanotechnol. **7**, 699 (2012).
[32] W. Zhao, Z. Ghorannevis, L. Chu, M. Toh, C. Kloc, P.-H. Tan, and G. Eda, ACS Nano **7**, 791 (2013).
[33] V. Podzorov, M. E. Gershenson, C. Kloc, R. Zeis, and E. Bucher, Appl. Phys. Lett. **84**, 3301 (2004).
[34] H. Yuan, M. S. Bahramy, K. Morimoto, S. Wu, K. Nomura, B.-J. Yang, H. Shimotani, R. Suzuki, M. Toh, C. Kloc, X. Xu, R. Arita, N. Nagaosa, and Y. Iwasa, Nat. Phys. **9**, 563 (2013).

[35] G. Seifert, H. Terrones, M. Terrones, G. Jungnickel, and T. Frauenheim, Phys. Rev. Lett. **85**, 146 (2000).
[36] M. Nath and C. N. R. Rao, Chem. Commun. **21**, 2236 (2001).
[37] U. Sivan and Y. Imry, Phys. Rev. B **33**, 551 (1986).
[38] Y. M. Blanter and M. Büttiker, Phys. Rep. **336**, 1 (2000).
[39] Y. Wei, B. Wang, J. Wang, and H. Guo, Phys. Rev. B **60**, 16900 (1999).
[40] G. Iannaccone, G. Lombardi, M. Macucci, and B. Pellegrini, Phys. Rev. Lett. **80**, 1054 (1998).
[41] Y. M. Blanter and M. Büttiker, Phys. Rev. B **59**, 10217 (1999).
[42] D. Li, L. Zhang, F. M. Xu, and J. Wang, Phys. Rev. B **85**, 165402 (2012).
[43] M. Büttiker, A. Prêtre, and H. Thomas, Phys. Rev. Lett. **70**, 4114 (1993).
[44] B. Wang, J. Wang, and H. Guo, Phys. Rev. Lett. **82**, 398 (1999).
[45] M. Büttiker, J. Phys.: Condens. Matter **5**, 9361 (1993).
[46] J.-N. Zhuang, L. Zhang, and J. Wang, AIP Advances **1**, 042180 (2011).
[47] J. Taylor, H. Guo, and J. Wang, Phys. Rev. B **63**, 245407 (2001).
[48] D. Waldron, P. Haney, B. Larade, A. MacDonald, and H. Guo, Phys. Rev. Lett. **96**, 166804 (2006).
[49] J. P. Perdew, K. Burke, and M. Ernzerhof, Phys. Rev. Lett. **77**, 3865 (1996).
[50] N. Troullier and J. L. Martins, Phys. Rev. B **43**, 1993 (1991).
[51] G. Kresse and J. Hafner, Phys. Rev. B **47**, 558 (1993).
[52] G. Kresse and J. Furthmller, Comput. Mater. Sci. **6**, 15 (1996).
[53] L. Fernández-Seivane, M. A. Oliveira, S. Sanvito, and J. Ferrer, J. Phys.: Condens. Matter **18**, 7999 (2006).
[54] L. Grigorian, G. U. Sumanasekera, A. L. Loper, S. L. Fang, J. L. Allen, and P. C. Eklund, Phys. Rev. B **60**, R11309 (1999).